Journal of Applied Physics

RESEARCH ARTICLE | OCTOBER 18 2024

# Domain evolution in $BiFeO_3$ epitaxial nanoisland array via post-annealing

Guo Tian ✉ ; Xingchen Zhang; Gui Wang; Jun Jin ; Houlin Zhou; Ji-Yan Dai ✉ ; Jun-Ming Liu ; Xingsen Gao ✉



*J. Appl. Phys.* 136, 154104 (2024)
https://doi.org/10.1063/5.0237974









AIP Publishing

Journal of Applied Physics ARTICLE pubs.aip.org/aip/jap

# Domain evolution in $BiFeO_3$ epitaxial nanoisland array via post-annealing

Cite as: J. Appl. Phys. **136**, 154104 (2024); doi: 10.1063/5.0237974
Submitted: 8 September 2024 · Accepted: 6 October 2024 ·
Published Online: 18 October 2024

View Online Export Citation CrossMark

Guo Tian,[1,2,a] Xingchen Zhang,[1] Gui Wang,[1] Jun Jin,[1] Houlin Zhou,[1] Ji-Yan Dai,[2,a] Jun-Ming Liu,[1,3] and Xingsen Gao[1,a]

## AFFILIATIONS

[1]Guangdong Provincial Key Laboratory of Quantum Engineering and Quantum Materials and Institute for Advanced Materials, South China Academy of Advanced Optoelectronics, South China Normal University, Guangzhou 510006, China
[2]Department of Applied Physics, Hong Kong Polytechnic University, Hong Kong, China
[3]Laboratory of Solid-State Microstructures and Innovation Center of Advanced Microstructures, Nanjing University, Nanjing 210093, China

[a]**Authors to whom correspondence should be addressed:** guotian@m.scnu.edu.cn; jiyan.dai@polyu.edu.hk; and xingsengao@scnu.edu.cn

## ABSTRACT

We describe the impact of post-annealing on ferroelectric-domain structures in arrays of $BiFeO_3$ (BFO) epitaxial nanoislands, which exhibit a domain evolution from an initial 71° stripe/vortex domains to center-convergent topological domains. These results suggest that the increase and redistribution of charged defects, e.g., oxygen vacancies, in BFO nanoislands play a crucial role in driving the formation of center-type domain structures. The observation of defect-driven domain evolution in BFO nanoislands provides a path for further exploring their formation mechanism, topological properties, novel functionalities, and potential applications.





## I. INTRODUCTION

Ferroelectric materials have garnered considerable attention for their potential applications in memories, sensors, actuators, and memristors.[1–10] The structure and dynamic characteristics of ferroelectric domains in nanoscale ferroelectric materials can greatly impact their physical properties and device functionalities, such as electrical conductivity,[11–14] photovoltaic response,[15] and magnetoelectric coupling.[16–19] These characteristics offer the opportunity to design materials and devices utilizing domain engineering techniques.[20,21] Therefore, the exploration of nanoscale domain structures and their associated physical properties is expected to bring new material and device solutions for the post-Moore era in information technology.[22]

Many efforts have been dedicated to exploring ferroelectric nanostructures due to their novel domain states and physical properties induced by size effects.[23–25] A series of exotic domains have been discovered in ferroelectric nanodots or nanoislands, e.g., vortices,[26,27] flux-closure domains,[28] bubble domains,[29,30] and center domains.[31–37] In particular, the electric-field-controlled reversible switching and enhanced conductivity of the center-type domains observed in ferroelectric nanoislands make them ideal candidates for future programmable nanoelectronic devices.[33] For instance, center-type topological domains can be reversibly switched between the divergent state with highly conductive confined walls and convergent state with insulating confined walls, demonstrating its potential for data storage applications with non-destructive readout of the topological center-domain state.[31] Based on conductive domain walls confined in center-type topological quadrant domains, Yang *et al.*[38] fabricated memory devices with a retention time of $10^6$ s and a fatigue resistance of $10^8$ switching cycles. These results are promising for achieving high-performance ferroelectric-domain-wall memory.

Considerable research has been focused on the structure and conductivity of domain walls. The mechanism of center-domain formation is complex, and research on their evolutionary processes remains limited. Possible formation mechanisms include

flexoelectric field, shear strains, and depolarization fields, or a combination of the above factors.[32,37,39] For instance, in self-assembled square-shape $BiFeO_3$ (BFO) nanoislands within a tetragonal BFO matrix, the center-domain textures are likely determined by the competition between depolarization energy and polarization–strain coupling.[31,32,37] However, in isolated rhombohedral-phase (R-phase) BFO nanoislands, depolarization field changes caused by defect charges may play a key role.[33,36] For center states created by applying electric bias via a nanoscale tip, the injected electrons trapped around the charged core/walls can help stabilize the domain states.[38] Hence, it is crucial to thoroughly investigate the effect of charged defects/electrons on the structure of center domains and explore their role in the formation process.

In this work, we subjected BFO nanoislands to post-annealing treatment in an $O_2$-poor atmosphere (inert $N_2$) and observed a domain structure evolution from 71° stripe/vortex domains to center-convergent topological domains, which indicates that the charged defects (e.g., oxygen vacancies) can significantly affect the formation of topological domains. This result might provide a new way to manipulate topological textures as well as further exploring their formation mechanism, physical phenomena, and application potentials.

## II. EXPERIMENTAL DETAILS

### A. Fabrication of BFO nanoislands array

As illustrated in Fig. S1 in the supplementary material, the ordered array of BFO epitaxial nanoislands was patterned via a template-assisted ion beam etching method, for which the details can be found in our previous work.[27] Before the nanopatterning process, high quality R-phase BFO epitaxial thin films were prepared by pulsed laser deposition (PLD) on the $SrRuO_3$ (SRO) buffered (001)-oriented $SrTiO_3$ (STO) substrate. The preparation process is summarized as follows: First, the nanosphere polystyrene (PS) template was transferred onto the BFO film to create an organized and tightly packed monolayer. After drying, the sample underwent plasma etching for around 30 min to reduce the size of the PS spheres. This was followed by an Ar+ ion beam etching process. Finally, the PS template was removed using a chloroform solution, revealing precisely arranged arrays of BFO nanoislands.

### B. Structure and morphology analysis

X-ray diffraction (XRD) and reciprocal space mapping (RSM) were used to measure the crystalline structures of samples. The morphology of the BFO nanoislands was characterized using the atomic force microscopy (AFM) mode of an Asylum Research MFP-3D scanning probe microscope.

### C. Piezoresponse force microscopy (PFM) characterizations

The local piezoresponse loops and vector polarization maps of the BFO nanoislands were obtained using the piezoresponse force microscopy (PFM) mode. In constructing the domain structures of the BFO nanoislands, an angle-resolved PFM technique was adopted with two lateral PFM images obtained at different sample orientation angles. Cr–Pt-coated conducting tips acted as the top electrode in all the AFM and PFM measurements.

## III. RESULTS AND DISCUSSION

Prior to nanopatterning, we examined the domain structure of an (001)-oriented epitaxial R-BFO film with a thickness of ~30 nm. As shown in Figs. 1(a) and 1(b), the domain structure of the as-grown thin film displays a typical 71° stripe domain pattern, reflected in the lateral PFM images shown in Fig. 1(b). The thin films were then etched into an array of nanoislands with a diameter of 400 nm and a height of 30 nm, shown in the AFM image of Fig. 1(c). Figure S2 in the supplementary material shows the morphology and PFM images of the prepared BFO films, along with that of etched nanoislands with diameters of 400 and 150 nm, respectively. The XRD $\theta$–$2\theta$ spectra, as shown in Fig. 1(d), reveal distinctive and well-defined peaks corresponding to the (001) and (002) orientations of R-BFO (referenced to the pseudo-cubic unit cell), SRO, and the STO substrate. The epitaxial structure was further confirmed through a reciprocal space map (RSM) analysis around the STO (103) diffraction peak, as shown in Fig. 1(e). From the XRD and RSM data, the lattice constants for BFO are $a = 0.392$ nm (in-plane spacing) and $c = 0.405$ nm (out-of-plane spacing), indicating an in-plane compressive strain due to epitaxy.

Oxygen vacancies in oxide ferroelectrics can be strongly coupled to the polar order via local strain and electric fields, producing and stabilizing exotic polarization patterns.[40] The oxygen vacancy content of the BFO nanoislands was subsequently modified by post-annealing in an $O_2$-poor atmosphere (inert $N_2$ in this work) at various temperatures. To verify the existence of oxygen vacancy, we measured the x-ray photoelectron spectroscopy (XPS) of different BFO nanoislands. Figure S3(a) in the supplementary material shows the wide scan survey spectrum for the pristine and $N_2$ post-annealed nanoislands, respectively. Figure 2(a) shows the high-resolution spectra of Bi 4f of these two samples. In Fig. 2(a), it can be seen that the pristine BFO nanoislands exhibit two clearly peaks at around 163.2 and 157.9 eV. These peaks can be attributed to the binding energies of Bi $4f_{5/2}$ and Bi $4f_{7/2}$, respectively, which indicate the existence of the $Bi^{3+}$ valence state.[41] In Fig. 2(b), the binding energies of Fe 2p (Fe $2p_{3/2}$ and Fe $2p_{1/2}$) along with a satellite peak, indicate that the Fe element was present in the $Fe^{3+}$ valence state in the pristine BFO nanoislands.[42] After post-annealing in $N_2$, it is found that the peaks of Bi and Fe in the spectra of pristine BFO nanoislands shifted toward high binding energy. The shift of these XPS peaks can be attributed to the formation of oxygen vacancy, which could increase the equilibrium electron density and, thus, make the energies increase.[43] The O 1s core-level XPS spectra of both the pristine and post-annealed BFO nanoislands are displayed in Figs. 2(c) and 2(d), respectively. The main peak observed at around 529.3 eV in the spectrum is likely associated with lattice oxygen present in the BFO nanoislands. This peak signifies the existence of chemical bonding between metal and oxygen atoms in the structure. In contrast, the two smaller peaks observed around 531.2 and 532.4 eV are indicative of dangling bonds and surface absorbed oxygen, respectively.[43]

In XPS spectra of perovskite oxides, the appearance of dangling bonds and absorbed species (such as $O^-$, $O_2^-$, and $O^{2-}$) is

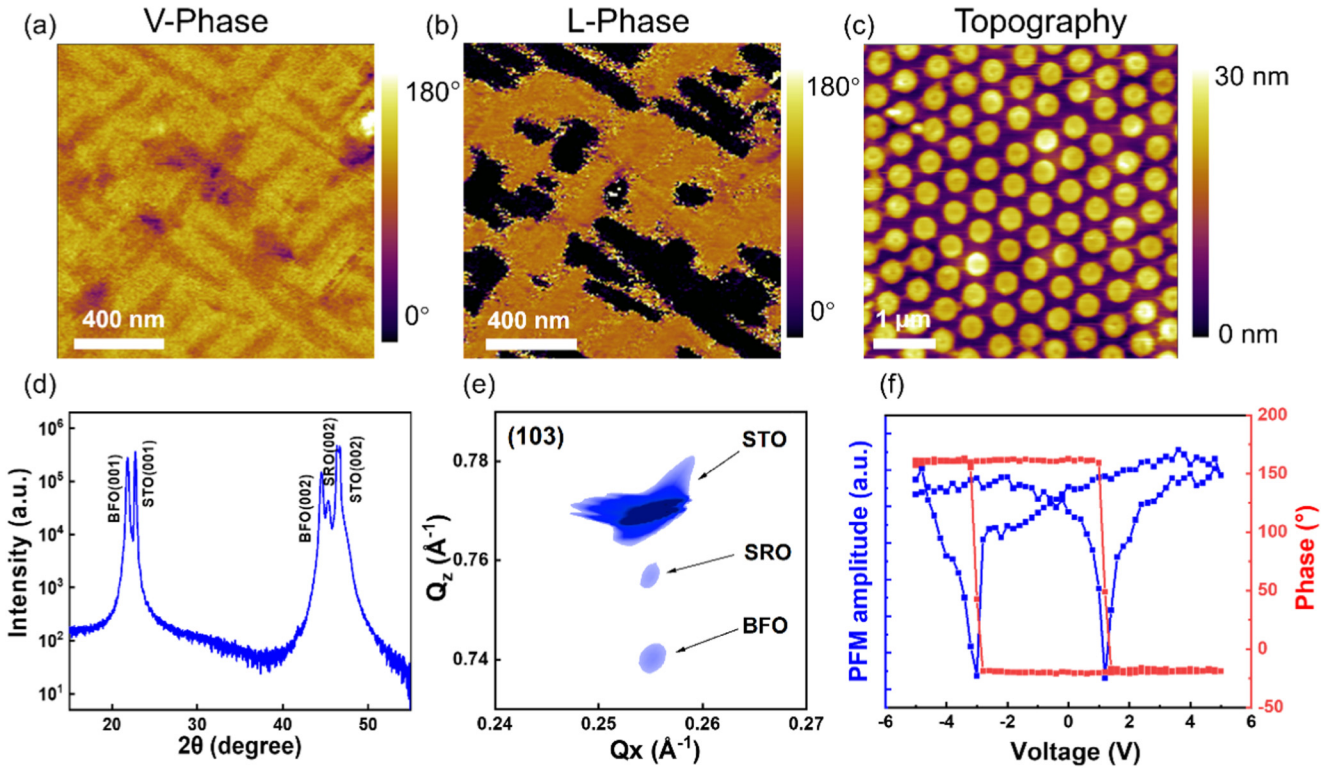


**FIG. 1.** Preparation and characterization of BFO nanoislands. (a) Vertical phase of and (b) lateral phase of the BFO film before etching. (c) Topography of an array of BFO nanoislands. (d) X-ray diffraction (XRD) and (e) reciprocal space mapping (RSM) of an as-fabricated sample with BFO nanoislands on an SRO/STO substrate. (f) Piezoresponse amplitude/phase–voltage hysteresis loops for a randomly selected nanoisland.

commonly linked to the creation of surface oxygen vacancies. One can approximate the concentration of surface oxygen vacancies based on the relative intensity ratio (RIR) of O 1s (lattice oxygen) to O 1s (dangling bonds and adsorbed oxygen).[44] The calculated RIR values of pristine nanoislands and $N_2$ post-annealing nanoislands are 1.51 and 1.14, respectively. These results suggest that the post-annealing process in $N_2$ leads to a significant increase in the concentration of oxygen vacancies in BFO nanoislands. We also calculated the RIR values of $O_2$ post-annealed nanoislands, as shown in Fig. S3(b) in the supplementary material, which is 1.82. These results suggest that the post-annealing process in $O_2$ leads to a decrease in the concentration of oxygen vacancies. It was known that removing an oxygen will leave with $2Fe^{2+}$. Thus, we calculated the relative intensity ratio of $Fe^{3+}/Fe^{2+}$ (R) in the nanoislands from the binding energies of Fe 2p, as shown in Fig. S4 in the supplementary material. The results show that the content of $Fe^{2+}$ increased after post-annealed in $N_2$, while decreased after post-annealed in $O_2$, which verified the change of oxygen vacancies in BFO nanoislands.

The ferroelectric properties of the BFO nanoislands were characterized by PFM. A saturated phase–voltage hysteresis loop and a butterfly-like amplitude–voltage loop are shown in Fig. 1(f), indicating a ferroelectric response. To ascertain the polarization orientation of these nanoislands before and after post-annealing, we executed the rotations of the sample by 0° and 90°. Vector PFM was employed to measure the in-plane and out-of-plane piezoelectric response signals, determining the polarization component along the x axis (⟨100⟩ direction) and y axis (⟨010⟩ direction). The morphology images shown in Figs. S5(e) and S5(i) in the supplementary material indicate that the surface structure of the nanoislands remains intact after post-annealing treatment in inert $N_2$ at 470 and 550 °C, respectively. However, as shown in Figs. S5(b) and S5(c), S5(f) and S5(g), and S5(j) and S5(k) in the supplementary material, the domain structure of the nanoislands undergoes significant alterations. As shown in Figs. S5(b) and S5(c) in the supplementary material, the lateral phase of most of the pristine states of nanoislands shows stripe-like dark-bright contrast, indicating stripe domain structures, which is consistent with our previous reports. After annealing for 40 min in a nitrogen atmosphere at 470 °C, some stripes transform into zigzag-like dark-bright contrast, as shown in Figs. S5(e) and S5(f) in the supplementary material. After further annealing the sample at 550 °C in nitrogen for 40 min, most of the zigzag-like contrast changed into a mixed state of half-black and half-white with a zigzag-like boundary. In order to better display the domain evolution process under different post-annealing conditions, we selected

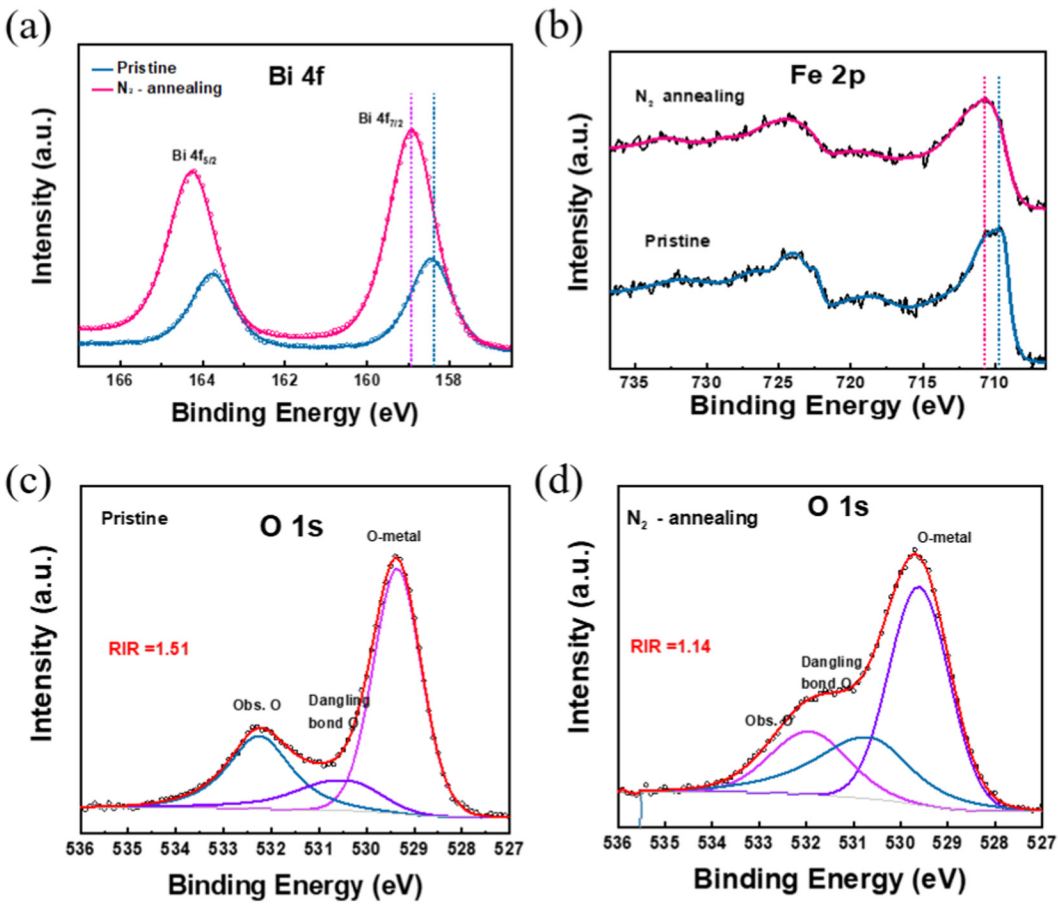


**FIG. 2.** High-resolution XPS of (a) Bi 4f and (b) Fe 2p for pristine and $N_2$-annealed BFO nanoislands, respectively; (c) and (d) O 1s core-level XPS spectra for different samples along with the split peaks and calculated relative intensity ratio (RIR) of O 1s (lattice oxygen)/O 1s (dangling bonds and adsorbed oxygen).

three representative nanoislands (marked with white, blue, and red circles) and reconstructed the lateral domain configurations, following the method by Kalinin *et al.*[45] As shown in Figs. S5(d), S5(h), and S5(l) in the supplementary material, the domain states of the nanoislands gradually evolve from the initial stripe domain to the zigzag domain (470 °C post-annealing) and ultimately to the center-domain states (550 °C post-annealing).

To obtain a more direct observation of the domain evolution in BFO nanoislands, we conducted a comparison between the domain structures of a nanoisland array region before and after post-annealing for 40 min in $N_2$ at 550 °C. As shown in Figs. 3(a)–3(c), the pristine states of these nanoislands exhibit a coexistence of stripe domains, and vortex and antivortex domains [see the left part of the vector map in Figs. 3(g) and 3(h)], consistent with our previous report.[27] After post-annealing at 550 °C, as mentioned earlier, both types of domains become half bright and half dark domain structures with zigzag domain walls, as shown in Figs. 3(d)–3(f). Two typical domain structures (circled in red and blue) were picked out, and the evolution before and after annealing was compared. The reconstructed vector polarization maps are shown in Figs. 3(g) and3(h). This analysis led to an intriguing discovery: The post-annealing domain structures tended to form head-to-head domain walls, forming a center-convergent topological domain. Similarly, we also conducted comparative analysis of the domain structures for another array after annealing at 470 and 550 °C. The results are shown in Fig. S6 in the supplementary material where the zigzag domain structure gradually shortens and becomes a square center-convergent topological domain. Detailed vector PFM images including the phase and amplitude captured at both two sample rotations are shown in supplementary Figs. S7, S8, and S9 in the supplementary material.

The combination of changes in the depolarization field and flexoelectric effects generated the center-type topological domains in the BFO nanoislands, wherein the defect charges (such as oxygen vacancy) resulting from $N_2$-annealing assume a key role. In the pristine state, the BFO nanoislands show out-of-plane downward polarization, indicating the downward interfacial build-in field from the SRO/BFO layers, as well as an upward depolarization

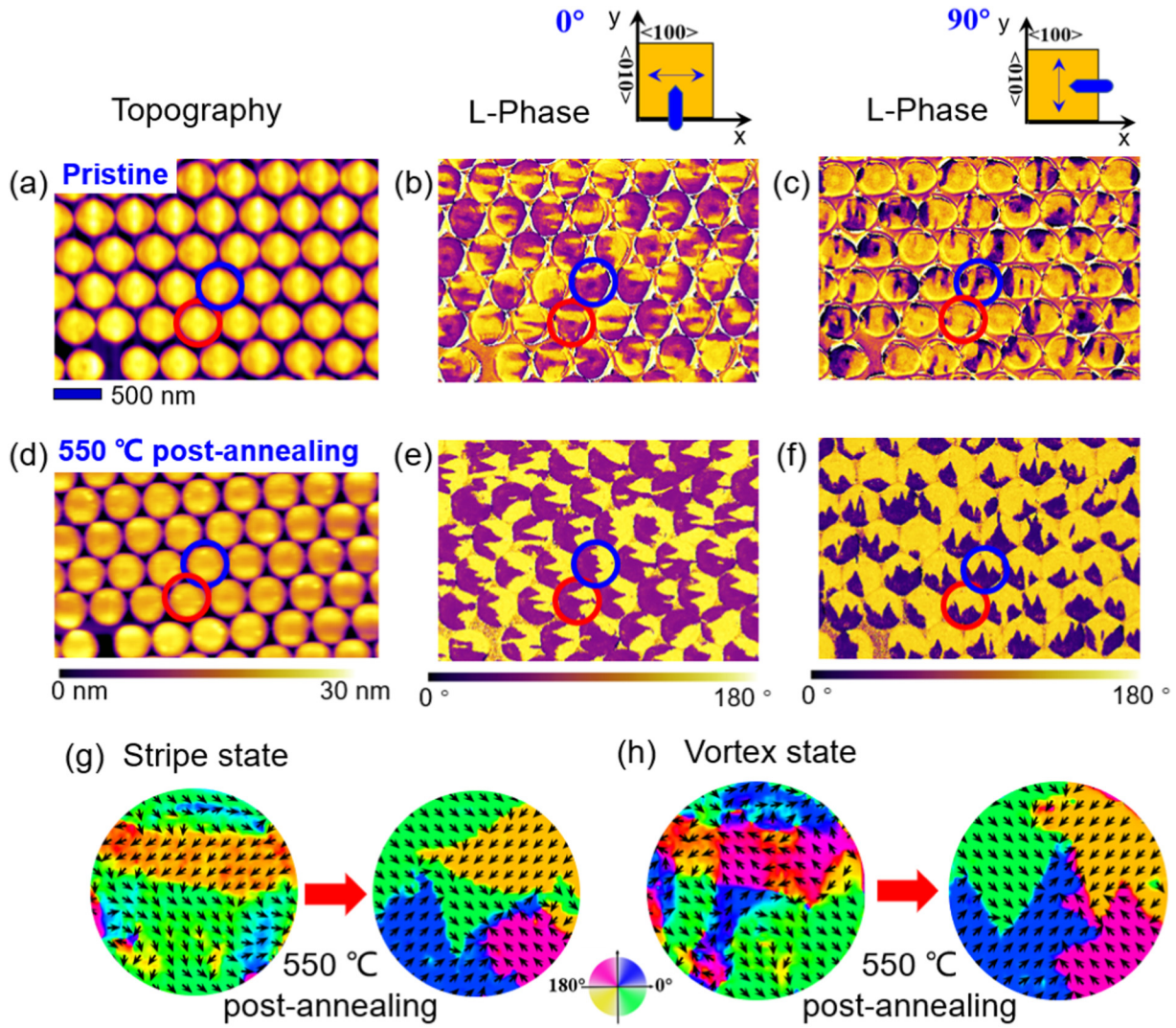


**FIG. 3.** AFM and PFM images of an array of BFO nanoislands before and after 550 °C post-annealing in an $N_2$ atmosphere. (a)–(c) PFM characterization of nanoislands before 550 °C post-annealing, including (a) topography, (b) in-plane phase at 0°, and (c) in-plane phase at 90°. The orientations of each scan direction are marked above the corresponding column. The scale bar in (a) represents 500nm. (d)–(f) PFM characterization of nanoislands after 550 °C annealing, including (d) topography, (e) in-plane phase at 0°, and (f) in-plane phase at 90°. (g) Map of the in-plane polarization distribution of the nanoisland marked with a red circle in (a)–(f). The initial state of the nanoisland is a stripe state. (h) Map of the in-plane polarization distribution of the nanoisland marked with a blue circle in (a)–(f). The initial state of the nanoisland is a vortex state.

field. After post-annealing in $N_2$, the oxygen vacancy concentration increases significantly. Considering a poor oxidizing environment and the diffusivity of oxygen vacancies at such a high temperature, oxygen vacancies in the nanoisland may be further attracted to the top and side surfaces by their affinity to oxygen on the free surface.[40] In this case, the distribution of oxygen vacancies in the $N_2$-annealed BFO nanoisland should be more concentrated on the top and side surfaces. The population of positively charged oxygen vacancies at the top surface of the nanoisland can generate an additional built-in electric field that points downward toward the bottom electrode. The local build-in fields can be revealed by piezoresponse hysteresis loops. As shown in Fig. S10 in the supplementary material, the piezoresponse loops were measured by PFM at different BFO nanoisland samples, from which we extracted their corresponding coercive fields and build-in fields. The pristine state of the BFO nanoisland exhibits an asymmetric hysteresis loop shifting toward the negative field side, suggesting the interfacial build-in field pointing to the bottom electrode. The corresponding build-in field can be then estimated from the difference of the positive coercive field and the negative coercive field, which can be

calculated as about −1.2 V. While the hysteresis loop of the $N_2$-annealed BFO nanoisland also shifted in the same direction, it exhibited a much larger average built-in field of about −2.8 V. The results obtained clearly demonstrate the presence of an additional factor within the $N_2$-annealed nanoisland, which subsequently produces an extra field to further enhance the build-in field, resulting in the alignment of the polarization after annealing. It has been reported that oxygen vacancy can lead to lattice expansion, as the cations are forced outward. Thus, we measured the XRD of the samples under different annealing conditions. However, it seems that the change in the lattice constant is too small.

It is worth mentioning that the local accumulation of oxygen vacancies can result in the formation of charged domain walls.[46] Furthermore, the BFO nanoislands possess n-type ferroelectric properties due to the presence of electronic carriers (electrons liberated from oxygen vacancies). This results in the head-to-head charge domain walls (H–H CDWs) containing positive bound charges that are more easily screened, leading to lower energy levels compared to the negative bound charges found in the tail-to-tail charge domain walls (T–T CDWs). Therefore, H–H CDWs are observed to form in the $N_2$-annealed nanoislands in our experiments. Combined with the constraint from the round nanoisland structure, provide geometry and strain boundary conditions that energetically promote the formation of center-convergent topological domains.

The characterization of domain structure evolution induced by $N_2$-annealing is also confirmed in smaller-sized BFO nanoislands. When the diameter of BFO nanoislands is decreased to 150 nm, single domains are found along with a small amount of stripe domains, as shown in Figs. S2(g)–S2(i) in the supplementary material. After annealing the sample for 40 min in $N_2$ at 550 °C, head-to-head domain walls form, as reflected by the lateral PFM images in Fig. 4. In comparison, we measured the domain states of the BFO nanoislands after post-annealing in $O_2$, and it was found that the majority of the nanoislands maintain the 71° stripe domain patterns, which are similar to the pristine states.

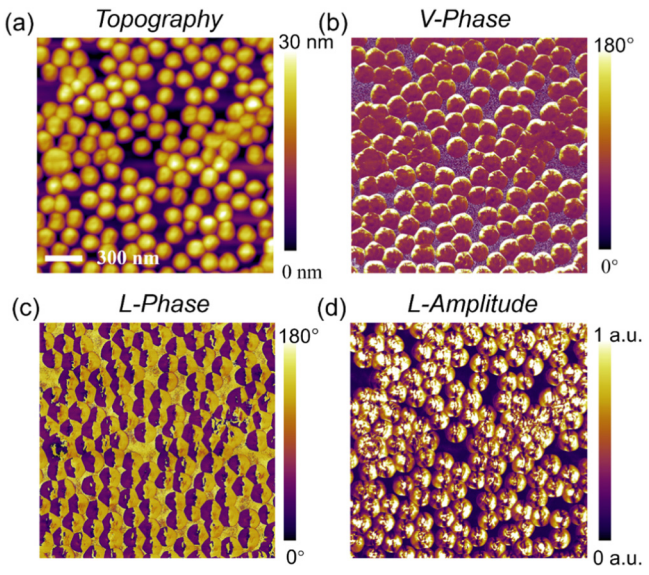


**FIG. 4.** PFM image of BFO nanoislands with a diameter of 200 nm after post-annealing at 550 °C in an $N_2$ atmosphere. (a) Topography, (b) out-of-plane phase, (c) in-plane phase, (d) in-plane amplitude. The scale bar is 300 nm.

Finally, we provide a schematic process for domain evolution in BFO epitaxial nanoislands via post-annealing in $N_2$. First, there are two different domain structures in the pristine states, the stripe and the vortex, as shown in Fig. S11 in the supplementary material. The stripe state appears as a stripe domain when measured at 0° and as a monodomain when measured at 90°, with 71° domain walls. When annealed at 470 °C, the shape of domains becomes sharper, forming zigzag-like stripe, and antiparallel domains grow in the ⟨010⟩ direction. In some areas, a head-to-head polarization distribution occurs. We refer to this type of domain as zigzag domains. After annealing at 550 °C, the sharp domain walls of the zigzag domains undergo contraction, exhibiting a half bright and half dark domain structure with zigzag walls visible in both 0° and 90° measurements, forming a center-type domain. Different from stripe domains, the vortex state exhibits stripes in both 0° and 90° measurements. By reconstructing the in-plane polarization direction, it can be seen that some small vortex domains have formed. After annealing at 470 °C, the stripes in the ⟨100⟩ and ⟨010⟩ directions become sharp, manifesting as zigzag domains, and some vortex domains begin to disappear. After annealing at 550 °C, the vortex domains transform into center-type domains with polarization directions pointing toward the center.

## IV. CONCLUSIONS

In summary, we present the observations of domain structure evolution in epitaxial BFO nanoislands on the STO substrate induced by post-annealing treatment in an inert $N_2$ atmosphere at various temperatures. By using vector PFM characterization, we compared the domain structures before and after the annealing of BFO nanoislands in the same region and found the evolution progresses from initial stripe/vortex domains to final center-convergent domains. The mechanism of the domain evolution is attributed to alteration of the distribution of depolarization field in nanoislands by the concentration of oxygen defects induced during annealing in $N_2$. These findings provide insights into the mechanism of domain formation in center-type topological domains.

## SUPPLEMENTARY MATERIAL

See the supplementary material for details on the structure and domain states of the BFO nanoislands.

## ACKNOWLEDGMENTS

The authors thank Professor Caroline Ross for helpful discussions. The authors acknowledge the National Key Research and Development Programs of China (No. 2022YFB3807603), the National Natural Science Foundation of China (NNSFC) (Nos. U22A20117 and 92163210), the Guangdong Basic and Applied Basic Research Foundation (Nos. 2023B1515130003 and 2024A1515011608), and the Science and Technology Projects in

Guangzhou (No. 202201000008), and G.T. acknowledges the support from Hong Kong Scholar Program (No. XJ2022004).

## AUTHOR DECLARATIONS

### Conflict of Interest

The authors have no conflicts to disclose.

### Author Contributions

G. T., X. Z., and G. W. contributed equally to this work.

**Guo Tian:** Conceptualization (equal); Data curation (equal); Investigation (equal); Writing – original draft (equal); Writing – review & editing (equal). **Xingchen Zhang:** Data curation (equal); Formal analysis (equal). **Gui Wang:** Data curation (equal); Formal analysis (equal). **Jun Jin:** Data curation (supporting); Formal analysis (supporting). **Houlin Zhou:** Data curation (supporting); Formal analysis (supporting). **Ji-Yan Dai:** Writing – original draft (supporting); Writing – review & editing (supporting). **Jun-Ming Liu:** Writing – review & editing (supporting). **Xingsen Gao:** Funding acquisition (equal); Investigation (equal); Project administration (equal); Writing – review & editing (equal).

## DATA AVAILABILITY

The data that support the findings of this study are available from the corresponding authors upon reasonable request.

## REFERENCES

[1]J. F. Scott, "Applications of modern ferroelectrics," Science **315**, 954 (2007).
[2]C. Catalan and J. F. Scott, "Physics and applications of bismuth ferrite," Adv. Mater. **21**, 2463 (2009).
[3]S. Q. Chen, S. Yuan, Z. P. Hou, Y. L. Tang, J. Zhang, T. Wang, K. Li, W. W. Zhao, X. J. Liu, L. Chen, L. W. Martin, and Z. H. Chen, "Recent progress on topological structures in ferroic thin films and heterostructures," Adv. Mater. **33**, 2000857 (2021).
[4]I. J. Kim and J. S. Lee, "Ferroelectric transistors for memory and neuromorphic device applications," Adv. Mater. **35**, e2206864 (2023).
[5]L. W. Martin and A. M. Rappe, "Thin-film ferroelectric materials and their applications," Nat. Rev. Mater. **2**, 16087 (2017).
[6]E. Aksel and J. L. Jones, "Advances in lead-free piezoelectric materials for sensors and actuators," Sensors **10**, 1935 (2010).
[7]C. R. Bowen, H. A. Kim, P. M. Weaver, and S. Dunn, "Piezoelectric and ferroelectric materials and structures for energy harvesting applications," Energy Environ. Sci. **7**, 25 (2014).
[8]Z. Chen, W. Li, Z. Fan, S. Dong, Y. Chen, M. Qin, M. Zeng, X. Lu, G. Zhou, X. Gao, and J. M. Liu, "All-ferroelectric implementation of reservoir computing," Nat. Commun. **14**, 3585 (2023).
[9]Y. Lee, J. Park, S. Cho, Y. E. Shin, H. Lee, J. Kim, J. Myoung, S. Cho, S. Kang, C. Baig, and H. Ko, "Flexible ferroelectric sensors with ultrahigh pressure sensitivity and linear response over exceptionally broad pressure range," ACS Nano **12**(4), 4045 (2018).
[10]S. I. Shkuratov and C. S. Lynch, "A review of ferroelectric materials for high power devices," J. Materiomics **8**, 739 (2022).
[11]J. Seidel, L. W. Martin, Q. He, Q. Zhan, Y. H. Chu, A. Rother, M. E. Hawkridge, P. Maksymovych, P. Yu, M. Gajek, N. Balke, S. V. Kalinin, S. Gemming, F. Wang, G. Catalan, J. F. Scott, N. A. Spaldin, J. Orenstein, and R. Ramesh, "Conduction at domain walls in oxide multiferroics," Nat. Mater. **8**, 229 (2009).
[12]G. Tian, W. D. Yang, X. Song, D. F. Zheng, L. Y. Zhang, C. Chen, P. L. Li, H. Fan, J. X. Yao, D. Y. Chen, Z. Fan, Z. P. Hou, Z. Zhang, S. J. Wu, M. Zeng, X. S. Gao, and J.-M. Liu, "Manipulation of conductive domain walls in confined ferroelectric nanoislands," Adv. Funct. Mater. **29**, 1807276 (2019).
[13]D. F. Zheng, G. Tian, Y. D. Wang, W. D. Yang, L. Y. Zhang, Z. F. Chen, Z. Fan, D. Y. Chen, Z. P. Hou, X. S. Gao, Q. L. Li, and J. M. Liu, "Controlled manipulation of conductive ferroelectric domain walls and nanoscale domains in $BiFeO_3$ thin films," J. Materiomics **8**, 274 (2022).
[14]P. Maksymovych, A. N. Morozovska, P. Yu, E. A. Eliseev, Y. H. Chu, R. Ramesh, A. P. Baddorf, and S. V. Kalinin, "Tunable metallic conductance in ferroelectric nanodomains," Nano Lett. **12**, 209 (2012).
[15]J. Seidel, D. Fu, S. Y. Yang, E. Alarcón-Lladó, J. Q. Wu, R. Ramesh, and J. W. Ager III, "Efficient photovoltaic current generation at ferroelectric domain walls," Phys. Rev. Lett. **107**, 126805 (2011).
[16]F. Zavaliche, H. Zheng, L. Mohaddes-Ardabili, S. Y. Yang, Q. Zhan, P. Shafer, E. Reilly, R. Chopdekar, Y. Jia, P. Wright, D. G. Schlom, Y. Suzuki, and R. Ramesh, "Electric field-induced magnetization switching in epitaxial columnar nanostructures," Nano Lett. **5**, 1793 (2005).
[17]S. H. Xie, F. Y. Ma, Y. M. Liu, and J. Y. Li, "Multiferroic $CoFe_2O_4$–Pb$(Zr_{0.52}Ti_{0.48})O_3$ core-shell nanofibers and their magnetoelectric coupling," Nanoscale **3**, 3152 (2011).
[18]Y. X. Li, Z. C. Wang, J. J. Yao, T. N. Yang, Z. G. Wang, J. M. Hu, C. L. Chen, R. Sun, Z. Tian, J. F. Li, L. Q. Chen, and D. Viehland, "Magnetoelectric quasi-(0-3) nanocomposite heterostructures," Nat. Commun. **6**, 6680 (2015).
[19]G. Tian, F. Y. Zhang, J. X. Yao, H. Fan, P. L. Li, Z. W. Li, X. Song, X. Y. Zhang, M. H. Qin, M. Zeng, Z. Zhang, J. J. Yao, X. S. Gao, and J. M. Liu, "Magnetoelectric coupling in well-ordered epitaxial $BiFeO_3/CoFe_2O_4/SrRuO_3$ heterostructured nanodot array," ACS Nano **10**, 1025 (2016).
[20]V. S. Kathavate, H. Sonagara, B. P. Kumar, I. Singh, and K. E. Prasad, "Tailoring nanomechanical properties of hard and soft PZT piezoceramics via domain engineering by selective annealing," Mater. Today Commun. **28**, 102495 (2021).
[21]H. Pan, J. Ma, J. Ma, Q. H. Zhang, X. Z. Liu, B. Guan, L. Gu, X. Zhang, Y. J. Zhang, L. L. Li, Y. Shen, Y. H. Lin, and C. W. Nan, "Giant energy density and high efficiency achieved in bismuth ferrite-based film capacitors via domain engineering," Nat. Commun. **9**, 1813 (2018).
[22]A. Lipatov, T. Li, N. S. Vorobeva, A. Sinitskii, and A. Gruverman, "Nanodomain engineering for programmable ferroelectric devices," Nano Lett. **19**, 3194 (2019).
[23]A. Gruverman and A. Kholkin, "Nanoscale ferroelectrics: Processing, characterization and future trends," Rep. Prog. Phys. **69**, 2443 (2006).
[24]H. Han, Y. Kim, M. Alexe, D. Hesse, and W. Lee, "Nanostructured ferroelectrics: Fabrication and structure–property relations," Adv. Mater. **23**, 4599 (2011).
[25]S. Yuan, Z. H. Chen, S. Prokhorenko, Y. Nahas, L. Bellaiche, C. H. Liu, B. Xu, L. Chen, S. Das, and L. W. Martin, "Hexagonal close-packed polar-skyrmion lattice in ultrathin ferroelectric $PbTiO_3$ films," Phys. Rev. Lett. **130**, 226801 (2023).
[26]B. J. Rodriguez, X. S. Gao, L. F. Liu, W. Lee, I. I. Naumov, A. M. Bratkovsky, D. Hesse, and M. Alexe, "Vortex polarization states in nanoscale ferroelectric arrays," Nano Lett. **9**, 1127 (2009).
[27]G. Tian, D. Y. Chen, H. Fan, P. L. Li, Z. Fan, M. H. Qin, M. Zeng, J. Y. Dai, X. S. Gao, and J.-M. Liu, "Observation of exotic domain structures in ferroelectric nanodot arrays fabricated via a universal nanopatterning approach," ACS Appl. Mater. Interfaces **9**, 37219 (2017).
[28]A. Schilling, D. Byrne, G. Catalan, K. G. Webber, Y. A. Genenko, G. S. Wu, J. F. Scott, and J. M. Gregg, "Domains in ferroelectric nanodots," Nano Lett. **9**, 3359 (2009).
[29]F. Y. Zhang, G. Tian, L. N. Zhao, X. S. Gao, and J. Y. Li, "Bubble domain evolution in well-ordered $BiFeO_3$ nanocapacitors," J. Adv. Dielectr. **13**, 2345003 (2023).
[30]X. C. Zhang, H. Y. Chen, G. Tian, W. D. Yang, Z. Fan, Z. P. Hou, D. Y. Chen, M. Zeng, M. H. Qin, J. W. Gao, X. S. Gao, and J. M. Liu, J. Materiomics **9**, 626 (2023).

[31]J. Ma, J. Ma, Q. H. Zhang, R. C. Peng, J. Wang, C. Liu, M. Wang, N. Li, M. F. Cheng, X. X. Cheng, P. Gao, L. Gu, L. Q. Chen, P. Yu, J. X. Zhang, and C. W. Nan, "Controllable conductive readout in self-assembled, topologically confined ferroelectric domain walls," Nat. Nanotechnol. **13**, 947 (2018).
[32]K.-E. Kim, S. Jeong, K. Chu, J. H. Lee, G.-Y. Kim, F. Xue, T. Y. Koo, L.-Q. Chen, S.-Y. Choi, R. Ramesh, and C.-H. Yang, "Configurable topological textures in strain graded ferroelectric nanoplates," Nat. Commun. **9**, 403 (2018).
[33]Z. W. Li, Y. J. Wang, G. Tian, P. L. Li, L. N. Zhao, F. Y. Zhang, J. X. Yao, H. Fan, X. Song, D. Y. Chen, Z. Fan, M. H. Qin, M. Zeng, Z. Zhang, X. B. Lu, S. J. Wu, C. H. Lei, Q. F. Zhu, J. Y. Li, X. S. Gao, and J.-M. Liu, "High-density array of ferroelectric nanodots with robust and reversibly switchable topological domain states," Sci. Adv. **3**, e1700919 (2017).
[34]M. J. Han, Y. J. Wang, Y. L. Tang, Y. L. Zhu, J. Y. Ma, W. R. Geng, M. J. Zou, Y. P. Feng, N. B. Zhang, and X. L. Ma, "Shape and surface charge modulation of topological domains in oxide multiferroics," J. Phys. Chem. C **123**, 2557 (2019).
[35]H. Y. Chen, G. Tian, W. D. Yang, Z. H. Mo, L. Y. Zhang, Y. Y. Chen, C. Chen, Z. P. Hou, D. Y. Chen, Z. Fan, X. S. Gao, and J.-M. Liu, "Complex center-type topological domain in ferroelectric nanoislands of rhombohedral $Pb(Zr_{0.7},Ti_{0.3})O_3$," J. Appl. Phys. **128**, 224103 (2020).
[36]X. C. Zhang, Y. H. Guo, G. Tian, Z. Q. Song, C. Chen, W. D. Yang, Z. P. Hou, D. Y. Chen, Z. Fan, G. F. Zhou, J.-M. Liu, and X. S. Gao, "Observation of center-type quad-domain structures in ordered $BiFeO_3$ nanoisland arrays fabricated via mask-assisted pulsed laser deposition," J. Appl. Phys. **133**, 134103 (2023).
[37]G. Tian, X. Yi, Z. Q. Song, W. D. Yang, J. B. Xian, J. Jin, S. Ning, Z. P. Hou, D. Y. Chen, Z. Fan, M. H. Qin, G. F. Zhou, J.-Y. Dai, X. S. Gao, and J.-M. Liu, "Templated growth strategy for highly ordered topological ferroelectric quad-domain textures," Appl. Phys. Rev. **10**, 021413 (2023).
[38]W. D. Yang, G. Tian, Z. Fan, H. Fan, Y. Zhao, H. Y. Chen, L. Y. Zhang, Y. D. Wang, Z. Fan, Z. P. Hou, D. Y. Chen, J. W. Gao, M. Zeng, X. B. Lu, M. H. Qin, X. S. Gao, and J.-M. Liu, "Nonvolatile ferroelectric-domain-wall memory embedded in a complex topological domain structure," Adv. Mater. **34**, 2107711 (2022).
[39]K.-E. Kim, Y.-J. Kim, Y. Zhang, F. Xue, G.-Y. Kim, K. Song, S.-Y. Choi, J.-M. Liu, L.-Q. Chen, and C.-H. Yang, "Ferroelastically protected polarization switching pathways to control electrical conductivity in strain-graded ferroelectric nanoplates," Phys. Rev. Mater. **2**, 084412 (2018).
[40]W. Peng, J. Mun, Q. Xie, J. Chen, L. Wang, M. Kim, and T. W. Noh, "Oxygen vacancy-induced topological nanodomains in ultrathin ferroelectric films," npj Quantum Mater. **6**, 48 (2021).
[41]F. Niu, D. Chen, L. S. Qin, N. Zhang, J. Y. Wang, Z. Chen, and Y. X. Huang, "Facile synthesis of highly efficient p–n heterojunction $CuO/BiFeO_3$ composite photocatalysts with enhanced visible-light photocatalytic activity," ChemCatChem. **7**, 3279–3289 (2015).
[42]T. Yamashita and P. Hayes, "Analysis of XPS spectra of $Fe^{2+}$ and $Fe^{3+}$ ions in oxide materials," Appl. Surf. Sci. **254**, 2441 (2008).
[43]Z. W. Li, H. Shen, G. Dawson, Z. Z. Zhang, Y. L. Wang, F. Nan, G. Song, G. N. Li, Y. J. Wu, and H. Liu, "Uniform arrays of centre-type topological domains in epitaxial ferroelectric thin films," J. Mater. Chem. C **10**, 3071 (2022).
[44]L. Qiao and X. F. Bi, "Direct observation of oxygen vacancy and its effect on the microstructure, electronic and transport properties of sputtered $LaNiO_{3-\delta}$ films on Si substrates," Thin Solid Films **519**, 943 (2010).
[45]S. V. Kalinin, B. J. Rodriguez, S. Jesse, J. Shin, A. P. Baddorf, P. Gupta, H. Jain, D. B. Williams, and A. Gruverman, "Vector piezoresponse force microscopy," Microsc. Microanal. **12**, 206 (2006).
[46]W. R. Geng, X. H. Tian, Y. X. Jiang, Y. L. Zhu, Y. L. Tang, Y. J. Wang, M. J. Zou, Y. P. Feng, B. Wu, W. T. Hu, and X. L. Ma, "Unveiling the pinning behavior of charged domain walls in $BiFeO_3$ thin films via vacancy defects," Acta Mater. **186**, 68 (2020).